A New Method to Design Trifurcated Optical Fiber Displacement Sensors

Gorka Zubia, *Graduate Student Member, IEEE*, Joseba Zubia, *Member, IEEE*, Josu Amorebieta, Gotzon Aldabaldetreku, and Gaizka Durana

***Abstract*—Trifurcated optical fiber displacement sensors (OFDSs) are increasingly used in industrial and aerospace applications. The critical element of the sensor is the fiber bundle. However, there is no straightforward method to calculate it from the working specifications of the sensor, the number of fibers needed, their size, and arrangement. This work presents a simple yet accurate method to design trifurcated OFDSs. The proposed method allows to derive the geometrical arrangement and size of the fibers from three simple equations, thus reducing significantly the difficulty and complexity of the OFDS design. Those three equations depend on the working point, working range, required sensitivity, and maximum size of the bundle. In this way, the proposed method will save valuable time for researchers and engineers who wish to design, fabricate, and use this type of OFDSs. The procedure is explained in detail with two examples. The results predicted by the model are compared with the experimental results of a bundle with identical fiber arrangement and dimensions. The results show good agreement with a deviation of less than 1% in the working range of the sensor.**

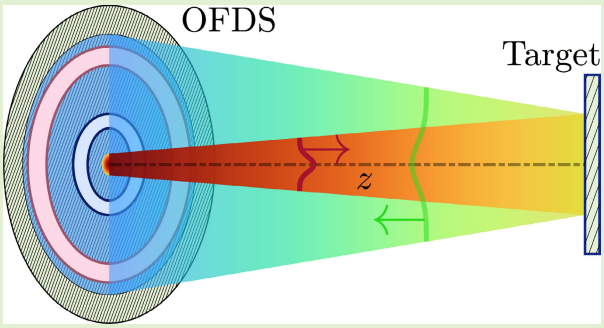

***Index Terms*— Design, fiber bundle, fiber optic sensors, intensity modulated optical sensor, method, optical fiber displacement sensor (OFDS), trifurcated.**

I. Introduction

HIGH precision metrology is essential in Industry 4.0 to monitor and improve the efficiency and versatility of factory processes [1], [2]. As a result, distance sensors are used in a wide range of applications to measure several parameters of interest such as the thickness, height, roughness, deformation, distortion, and gap between surfaces, for instance, [3], [4], [5]. To select the best-fitting device, we have to consider the application, the environment, and the required precision, as these factors are critical to determining the specifications of the sensor. A prime example of the latter can be acknowledged in the aeronautical turbine industry.

In that field, noncontact solutions are practically compulsory in order to carry out any metrology measurements, as heavy metallic pieces are rotating at high speed significantly close to each other [6]. To that end, the most popular alternatives are capacitive [7], inductive [8], ultrasonic [9], draw-wire, and optical sensors [10]. Among them, optical fiber displacement sensors (OFDSs) offer many advantages such as electromagnetic immunity, high response, speed, small size, great versatility, and easy installation, for example, [11], [12]. Within this group of sensors, OFDSs based on the reflection of optical intensity add two significant advantages: Firstly, as an optical fiber is used to transmit light to the monitored surface, the sensing heads can be installed in remote locations where direct laser light cannot reach, such as inside an aircraft turbine [13]. Secondly, since these sensors are often used in a differential configuration [14], they minimize several potential error sources due to reflective surface roughness, temperature variations, fluctuations in the emitting light source, and so on [15]. This approach is particularly useful for dynamic

Manuscript received 2 October 2023; revised 31 October 2023; accepted 25 November 2023. Date of publication 4 December 2023; date of current version 12 January 2024. This work was supported in part by the Grant I+D+i/PID2021-122505OB-C31, Grant TED2021-129959B-C21, Grant PDC2022-133053-C21, and Grant RTC2019-007194-4 through MCIN/AEI/10.13039/501100011033; in part by the "ERDF A way of making Europe"; in part by the "European Union Next Generation EU/PRTR"; in part by the Grant IT11452-22 and through the Basque Government; in part by the ELKARTEK 2023 under Grant μ4Smart-KK-2023/00016 and Grant Ekohegaz II-KK-2023/00051; and in part by the University of the Basque Country (UPV/EHU) Translight. The work of Gorka Zubia was supported by the Ph.D. fellowship from the Basque Government under Grant PRE_2022_2_0269. The associate editor coordinating the review of this article and approving it for publication was Dr. Sanjeev Raghuwanshi. *(Corresponding author: Gorka Zubia.)*

Gorka Zubia and Josu Amorebieta are with the Department of Applied Mathematics, University of the Basque Country UPV/EHU, 48013 Bilbao, Spain (e-mail: gorka.zubia@ehu.eus).

Joseba Zubia, Gotzon Aldabaldetreku, and Gaizka Durana are with the Department of Communications Engineering, University of the Basque Country UPV/EHU, 48013 Bilbao, Spain.

Digital Object Identifier 10.1109/JSEN.2023.3337311

© 2023 The Authors. This work is licensed under a Creative Commons Attribution-NonCommercial-NoDerivatives 4.0 License.
For more information, see https://creativecommons.org/licenses/by-nc-nd/4.0/

turbine testing, as the blades rotate and the reflective surface is constantly changing [16], [17].

The working range and sensitivity of OFDSs depend on their geometric structure, i.e., the number and transverse arrangement of fibers in a bundle [18], [19], [20], [21]. The typical OFDS configuration uses two adjacent optical fibers to transmit and receive the light signal through reflection [22]. However, this arrangement limits the amount of reflected light, which reduces the working range. Other configurations have been proposed, e.g., a pair of bent-tip optical fibers [23], a hemispherical arrangement of fibers, and even randomly distributed transmitting and receiving fibers [24], [25], or more recently, an OFDS based on a multicore fiber with seven cores hexagonally arranged [26].

Some authors prefer to use fibers or bundles that form an angle with one another and with the normal to the reflecting surface [27]. It has been found that setting the angle between the transmitting and receiving fibers to 20° increases the sensitivity up to 30 times over the conventional parallel fiber configuration. Asymmetric approaches like this are well-suited for angle measurement. For example, Sagrario and Mead [28] designed an OFDS using a square structure to perform both axial and angular displacement measurements; Khiat et al. [29] developed a fiber sensor with four receiving fibers around the transmitting one, for long-distance, high-resolution measurements. The drawback of such fiber bundles is that the sensor head increases proportionally with the angle. Additionally, many of these designs only allow the measurement of uniaxial rotation, that is, the ability to measure the tilt of the reflecting surface along just one axis [30]. In cases where the reflecting surface is neither homogeneous nor large and also vibrates, the angle is not maintained and changes rapidly. This applies to the measurement of tip clearance in aircraft turbines, where the reflecting surfaces are the blades and whose shape is twisted [31]. In these harsh environments, the angle measurement is not advantageous.

Therefore, the designs used to measure displacements in turbines are based on azimuthally symmetric arrangements, specifically, bundles of fibers arranged in concentric rings around a central emitting fiber. The most common designs are the trifurcated OFDSs [32], [33]. These are based on a fiber bundle with an emitting fiber in the center surrounded by two fiber rings at different radial distances. Typically, fiber bundles are custom-designed to meet the working range or sensitivity required by the specific application [34], [35]. Those parameters vary based on the number of fibers in each receiving ring, the size and numerical aperture of each fiber, or the radii of the fiber rings [36]. Various methods have been proposed to model the response of OFDSs: Geometric approximations [25], [37], ray tracing, Monte Carlo calculations [38] or Gaussian beam-based models. Of all these approaches, the one presented by Cao et al. [25] offers the widest range of possibilities, albeit it faces the drawback of requiring the implementation of 8 different formulas. The one based on a Gaussian or quasi-Gaussian beam has also excellent accuracy, but it is much simpler [39]. Anyway, designing the most suitable fiber bundle is a complex numerical task [25], [27], [38], [39] that the proposed approach in this article can greatly simplify.

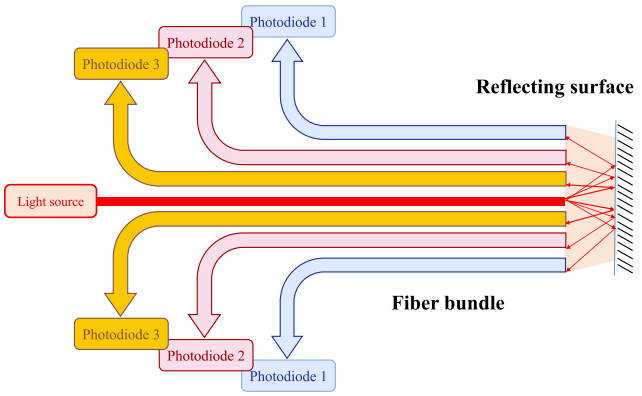

Fig. 1. Schematic of an OFDS. The constituent blocks are a light-emitting source, a fiber bundle to guide the light, and a receiver circuit to convert the collected light power into voltage.

Unlike prior methods, the method introduced here allows us to compute the bundle design that best fits the working specifications. The proposed method enables the deduction of the geometrical arrangement and fiber size within a bundle from three simple equations, thereby significantly reducing the difficulty and complexity of OFDS design, which can be time-consuming and expensive. The three equations only depend on the specifications defined at each application, namely, the working point and range, the required sensitivity, and the maximum size of the bundle. As a result, the proposed method will save valuable time for researchers and engineers who wish to design, fabricate, and use this type of OFDSs. This method can trivially be extended to designs with four (tetrafurcated), five (pentafurcated), or more fiber rings. The only limitation of the method is that it is restricted to the design of azimuthally symmetric bundles. The article is organized into four sections. Firstly, the mathematical model is presented. Secondly, the results obtained are analyzed. Thirdly, the design equations are derived. Finally, the model is validated by comparing the theoretical results with experimental ones.

II. Mathematical Model

The schematic of an OFDS is shown in Fig. 1. It comprises a light source, a fiber bundle, and a receiver. The light emitted by the light source is guided through the transmitting fiber to the reflecting surface. After reflection, the light is collected by the receiving fibers of the bundle. Each of these is connected to separate photodiodes, where the optical power is finally converted into voltage. The latter is a function of the distance between the bundle-tip and the reflective surface. The design of the bundle is critical, since the response of the OFDS is highly dependent on its geometric arrangement, i.e., the number, size, and distribution of the transmitting and receiving fibers [15], [20], [22], [27], [31].

The aim of this work is to develop a novel approach to design a trifurcated OFDS, taking the desired working point and range as input variables. For this purpose, we have built a toy model of the response of the sensor to understand the influence of each of the geometric parameters in order to fine-tune its response and meet the requirements of the specific application.

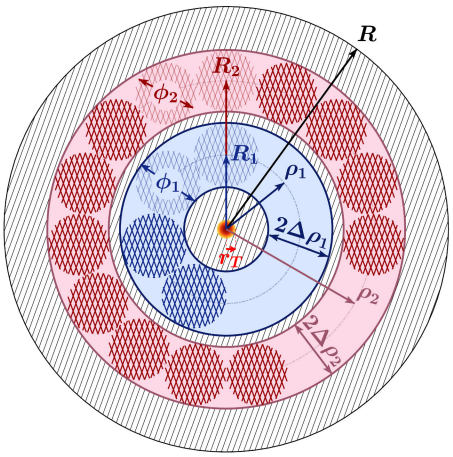

Fig. 2. Structure of a trifurcated fiber bundle with radius R, composed of a transmitting fiber of radius r_T located at the center, and two surrounding coaxial receiving rings. The positions of the rings are denoted as $\{\rho_1, \rho_2\}$, respectively. Their widths are labeled $\{\Delta\rho_1, \Delta\rho_2\}$. The diameters of the fibers $\{\phi_1, \phi_2\}$ correspond to the widths of the rings in the toy model, and their position equal the position of the fibers $\{R_1, R_2\}$.

Fig. 2 illustrates the geometry of the problem. It consists of a circular structure composed of a transmitting fiber located at the center of the bundle and two coaxial rings of receiving fibers surrounding it. The toy model replaces the discrete fiber rings with continuous homogeneous rings. This greatly simplifies the calculations while preserving all the bundle geometry parameters.

The positions of the rings and their widths are ρ_1, ρ_2, $\Delta\rho_1$, and $\Delta\rho_2$, respectively. The diameters of the fibers $\{\phi_1, \phi_2\}$ correspond to the widths of the rings in the toy model, and their position equals the positions of the fibers $\{R_1, R_2\}$. Other parameters are the radii of the transmitting fiber r_T and the bundle R. The validity of the toy model is confirmed in Section V.

We assume that the transmitting fiber is a single mode to reduce the modal noise at the output of the bundle [13]. Under this premise, we can approximate the irradiance at the output of the fiber as a Gaussian beam, using [40]

$$I(\rho, z) = I_0 \left[\frac{w_0}{w(z)}\right]^2 \exp\left(-2\frac{\rho^2}{w^2(z)}\right) = \frac{2P}{\pi w^2(z)} \exp\left(-2\frac{\rho^2}{w^2(z)}\right) \quad (1)$$

where $w(z)$ is the beamwidth, ρ is the radial distance from the propagation axis z and I_0 is the intensity of the beam at the origin. P refers to the total optical power transmitted by the beam and w_0 is the waist radius at its stretchiest point-where the intensity drops to $1/e^2 \approx 13.5\%$ of its maximum value. The beamwidth $w(z)$ spreads according to the formula

$$w(z) = w_0 \sqrt{1 + \left(\frac{z}{z_0}\right)^2}. \quad (2)$$

It reaches its minimum value w_0 at the bundle tip ($z = 0$). z_0 is the *Rayleigh distance*, defined as $z_0 = \pi w_0^2/\lambda$, which is the distance over which a beam can propagate without significantly diverging. The total light power emitted by the transmitting fiber, P, can easily be estimated as

$$\begin{aligned} P &= \int_0^\infty I(\rho) 2\pi r \, dr \\ &= 2\pi I_0 \left[\frac{w_0}{w(z)}\right]^2 \int_0^\infty \exp\left(-2\frac{\rho^2}{w^2(z)}\right) \rho \, d\rho \\ P &= \frac{\pi}{2} w_0^2 I_0. \end{aligned} \quad (3)$$

Since the light power remains constant at different z distances from the transmitting fiber-tip, both the peak intensity and the intensity distribution profile vary with z. In fact, on the beam axis, the intensity $I(0, z)$ drops to

$$I(0, z) = I_0 \frac{z_0^2}{z^2 + z_0^2}. \quad (4)$$

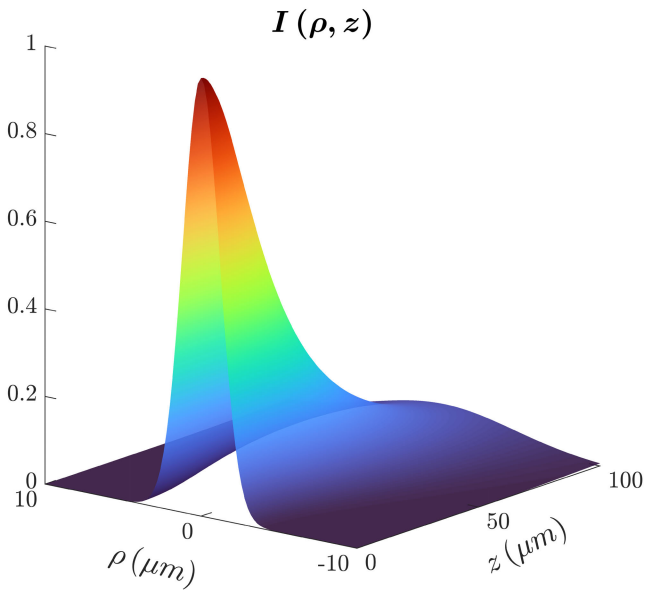

Fig. 3. Evolution of the light intensity of a Gaussian beam with z, taking $w_0 = 2.4$ μm and $z_0 = 27$ μm.

Fig. 3 shows the evolution of $I(\rho, z)$ with z.
For sufficiently large distances

$$\begin{aligned} z \gg z_0 \implies w(z) &\approx w_0 \frac{z}{z_0} \\ w(z) \approx z \tan\theta_0 &= z \tan(\arcsin \mathrm{NA}) \end{aligned} \quad (5)$$

being NA the numerical aperture of the transmitting fiber. The divergence angle θ_0 and w_0 are parameters that solely rely on the light source and transmitting fiber characteristics. Thus, once both are selected, θ_0 and w_0 remain constant.

At a certain distance of z, the light beam reaches a surface, reflects toward the receiver rings, and is collected after traveling a total distance of $2z$. The intensity at an infinitesimal ring of width $d\rho$ placed at a distance ρ from the fiber axis is

$$dI(\rho, 2z) = \frac{2\Gamma P}{\pi w^2(2z)} \exp\left(-2\frac{\rho^2}{w^2(2z)}\right) 2\pi\rho \, d\rho. \quad (6)$$

The ideal reflectance of the surface is Γ. Thus, the calculation of the detected irradiance in the ring located at a radial distance

ρ_1 with width $2\Delta\rho_1$ is straightforward

$$I(\rho_1, \Delta\rho_1, 2z) = \frac{2\Gamma P}{\pi w^2(2z)} \int_{\rho_1-\Delta\rho_1}^{\rho_1+\Delta\rho_1} \exp\left(-2\frac{\rho^2}{w^2(2z)}\right) 2\pi\rho\, d\rho$$

$$I(\rho_1, \Delta\rho_1, 2z) = 2\Gamma P \sinh\left(4\frac{\rho_1\Delta\rho_1}{w^2(2z)}\right) \exp\left(-2\frac{\rho_1^2+\Delta\rho_1^2}{w^2(2z)}\right). \tag{7}$$

Similarly, the measured irradiance in a second ring located at a distance ρ_2 and width $2\Delta\rho_2$ is

$$I(\rho_2, \Delta\rho_2, 2z) = 2\Gamma P \sinh\left(4\frac{\rho_2\Delta\rho_2}{w^2(2z)}\right) \exp\left(-2\frac{\rho_2^2+\Delta\rho_2^2}{w^2(2z)}\right). \tag{8}$$

Assuming that the two photodetectors collecting the light entering the two independent receiving rings have a typical quadratic response [6]

$$V_i = k_i 2\Gamma P \sinh\left(4\frac{\rho_i\Delta\rho_i}{w^2(2z)}\right) \exp\left(-2\frac{\rho_i^2+\Delta\rho_i^2}{w^2(2z)}\right) \tag{9}$$

where V_i is the output voltage of photodetector i, and k_i is a constant that includes the photodetector response and other factors such as noise, detector circuit gain, surface roughness, contamination, bends, etc. Consequently, the *responsivity* of the sensor, $\eta(z)$, is defined as the ratio of the optical intensities of its two receiving rings, i.e., V_2/V_1

$$\eta(z) = \frac{k_2 \sinh\left(4\frac{\rho_2\Delta\rho_2}{w^2(2z)}\right) \exp\left(-2\frac{\rho_2^2+\Delta\rho_2^2}{w^2(2z)}\right)}{k_1 \sinh\left(4\frac{\rho_1\Delta\rho_1}{w^2(2z)}\right) \exp\left(-2\frac{\rho_1^2+\Delta\rho_1^2}{w^2(2z)}\right)}$$

$$\eta(z) = k\frac{\sinh\left(4\frac{\rho_2\Delta\rho_2}{w^2(2z)}\right)}{\sinh\left(4\frac{\rho_1\Delta\rho_1}{w^2(2z)}\right)} \exp\left(-2\left(\frac{\rho_2^2+\Delta\rho_2^2-\rho_1^2-\Delta\rho_1^2}{w^2(2z)}\right)\right). \tag{10}$$

The constant k is defined as $k = k_2/k_1$. In the following (11), we assume that the response of both photodetectors is the same, so $k = 1$. Although the responsivity of the OFDS depends on four geometric parameters, we encompass these into just three: $\{A_1, A_2, q\}$. Thereby, (10) with (5) compacts to

$$\eta(z) = \frac{\sinh\left(\frac{A_2}{z^2\tan^2\theta_0}\right)}{\sinh\left(\frac{A_1}{z^2\tan^2\theta_0}\right)} \exp\left(-\frac{q}{z^2}\right) \tag{11}$$

where

$$\left.\begin{array}{l} A_1 = \rho_1\Delta\rho_1 \\ A_2 = \rho_2\Delta\rho_2 \\ q = \left(\rho_2^2+\Delta\rho_2^2-\rho_1^2-\Delta\rho_1^2\right)/2\tan^2\theta_0 \\ w(z) \approx z\tan\theta_0 \end{array}\right\} \text{Geometrical parameters.}$$

In Fig. 4, the responsivity is plotted along with the optical power collected by the inner and outer rings, $P_1(z)$ and $P_2(z)$, respectively. We applied a scaling factor of 2.5 to $P_1(z)$ and $P_2(z)$ to visualize the three functions together. Still, one can observe that the response of each ring is significantly smaller than the combined output. Furthermore, according to Fig. 4, the inner ring (red curve) demonstrates excellent performance at short distances due to a narrow but steep linear range, which

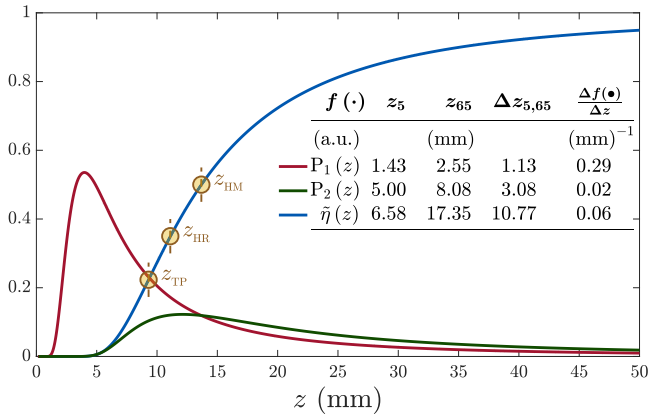

Fig. 4. Optical power collected by the inner-red, $P_1(z)$-and outer-green, $P_2(z)$-rings along with the responsivity-blue, $\eta(z)$. A scale factor of 2.5 was applied to $P_1(z)$ and $P_2(z)$ to display the three curves together. The table shows the linear ranges and their slopes. In yellow, some typical points of interest of $\eta(z)$ in mm: $z_{TP} = 9.3$, $z_{HR} = 12$, and $z_{HM} = 13.7$.

makes the sensor highly sensitive. Conversely, the outer ring (green curve), has a more extensive linear range at the cost of a loss of sensitivity, i.e., a slower growth of its response. This is because the received light is broadened and varies radially smoother. For the same reason, the outer ring receives less power, in this case, five times less than the inner ring.

However, we can also observe that taking the ratio between both curves results in a significantly improved response (blue curve). It is both greater in amplitude and larger in linear range. Thus, using a single-ring configuration has the only advantage of enabling shorter distance measurements. Nevertheless, as we have seen, working with a single ring has many disadvantages, mostly related to the inability to correct the emitting light source intensity fluctuations, ambient light, etc. Just as an example, if we define the linear range as the interval between 5% and 65% of the maximum value of the front slope of each curve, we obtain a linear range of $\Delta z_{5,65} = 1.13$ mm when working with the inner ring, and $\Delta z_{5,65} = 3.08$ mm for the outer. Finally, we can observe that the linear range of the responsivity-which combines the optical power of both rings-extends up to $\Delta z_{5,65} = 10.77$ mm.

The typical responsivity of the sensor is also presented in Fig. 4. It saturates at the limit value, when the distance to the reflector is sufficiently large

$$\lim_{z\to\infty} \eta(z) = \frac{\sinh\left(\frac{A_2}{z^2\tan^2\theta_0}\right)}{\sinh\left(\frac{A_1}{z^2\tan^2\theta_0}\right)} \exp\left(-\frac{q}{z^2}\right) = \frac{A_2}{A_1} = \frac{\rho_2\Delta\rho_2}{\rho_1\Delta\rho_1}. \tag{12}$$

For convenience, let us refer to this limit as p

$$p = \lim_{z\to\infty} \eta(z) = \frac{\rho_2\Delta\rho_2}{\rho_1\Delta\rho_1}. \tag{13}$$

According to (13), the saturation value of the sensor increases with the ratio of the receiving areas, A_2/A_1.

Fig. 5 illustrates how each term of the responsivity function contributes to the result (11), revealing that the hyperbolic sine term (11) in orange is significant only for small z values. For larger z values, it just multiplies the exponential by the limit p. In fact, the responsivity given by (11)

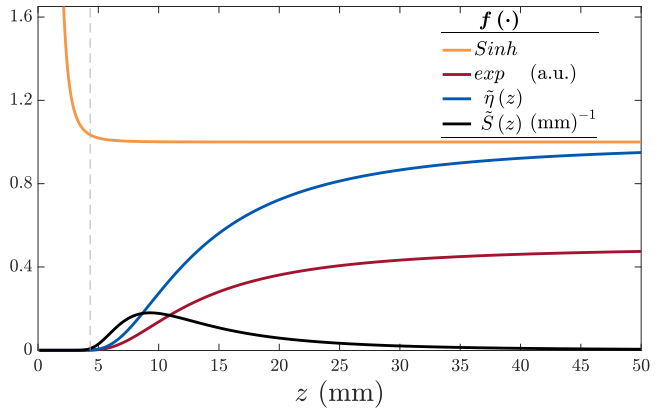

Fig. 5. Sensor response $\eta(z)$ in blue and $S(z)$ in black for the following design specifications (mm): $\rho_1 = 0.5$, $\rho_2 = 1.5$, $\Delta\rho_2 = 0.1$, and $\Delta\rho_2 = 0.15$. Also, $\theta_0 = 5°$, $q = 130$ mm^2, and $k = 1$. Contribution of the hyperbolic sines in orange; in red, the exponential one.

is indistinguishable from

$$\eta(z) = \frac{I(\rho_2, \Delta\rho_2, 2z)}{I(\rho_1, \Delta\rho_1, 2z)} \approx p \exp\left(-\frac{q}{z^2}\right). \tag{14}$$

A dashed vertical line has been added in Fig. 5 to indicate where the responsivity (blue line) is no longer zero. From that point on, the hyperbolic-sine-term barely changes and resembles a constant.

Another key parameter of the sensor is the *sensitivity*, §, defined as the slope of the responsivity

$$S(z) = \frac{d\eta(z)}{dz} = 2\frac{pq}{z^3} \exp\left(-\frac{q}{z^2}\right). \tag{15}$$

The sensitivity is maximum when the second derivative equals zero, i.e., solving for the *turning point*, z_{TP}, of the responsivity

$$S_{\max} = \left.\frac{d^2\eta(z)}{d^2z}\right|_{z=z_{\text{TP}}} = 0 \implies z_{\text{TP}} = \sqrt{\frac{2}{3}q}. \tag{16}$$

Thus, the value of the responsivity (14) at that point is

$$\eta(z_{\text{TP}}) = p \exp\left(-\frac{q}{z_{\text{TP}}^2}\right) \approx 0.22p. \tag{17}$$

An additional key point is the distance at which the responsivity reaches half its maximum value. We named it z_{HM}

$$\eta(z_{\text{HM}}) = \frac{1}{2}p. \tag{18}$$

Solving for z_{HM} yields to

$$z_{\text{HM}} = \sqrt{\frac{q}{\ln 2}} \approx 1.2\sqrt{q}. \tag{19}$$

Moreover, substituting (16) in (19) revealed that the relationship between z_{TP} and z_{HM} can be expressed as

$$z_{\text{HM}} = \sqrt{\frac{3}{2\ln 2}}\, z_{\text{TP}} = 1.47 z_{\text{TP}}. \tag{20}$$

In previous Fig. 4, we plotted the responsivity along with the proposed key parameters, namely: z_{TP}, z_{HM}, and z_{HR}. The latter is the distance point at half of the *working range* of the sensor. We assumed that the working range of the sensor is between the [5, 65]% of $\eta_{\max}$, which corresponds to the most linear region of the responsivity. So, z_{HR} will be at 35% of the maximum responsivity $\eta_{\max}$. As we will see in Section V, the working range may also be defined by fitting the responsivity to a straight line using Pearson's correlation coefficient.

III. Results and Discussion

After introducing the mathematical model in Section II, the next step is to analyze the results. Equations (11) and (14) characterize the responsivity of the sensor. Notice that it depends on the geometric parameters through two expressions

$$\rho_2^2 + \Delta\rho_2^2 - \rho_1^2 - \Delta\rho_1^2 \quad \text{and} \quad \frac{\rho_2\Delta\rho_2}{\rho_1\Delta\rho_1}.$$

The roles of $\{\rho_2, \Delta\rho_2\}$ and $\{\rho_1, \Delta\rho_1\}$ are symmetrical with respect to the responsivity. Also, changes in $\{\rho_2, \Delta\rho_2\}$ are equivalent, and the same is true for $\{\rho_1, \Delta\rho_1\}$. Therefore, we conducted our initial analysis of the responsivity through global changes in q and p. The dependence of the responsivity on those parameters is better exemplified in Fig. 6.

Fig. 6(a) shows the responsivity as a function of q and z for different values of p, from 1 to 5 in steps of 1. The green surface corresponds to $p = 5$, and the blue at the bottom corresponds to $p = 1$. Inspecting Fig. 6(a) leads us to two outcomes.

1) First, the shape of the curve does not change as the value of p increases. This implies that the position of the working point is independent of p, as evidenced in (16) and (19). However, it does change the scale and slope of the curve and, therefore, the sensitivity in the neighborhood of the working point.
2) Second, the analysis of the responsivity reveals two simultaneous effects: on the one hand, the reduction of the parameter q shifts the turning point to smaller values; thus if we want to work at short distances, the parameter q must be small. This fact is supported by (16). On the other hand, it shows that this decrement of q is associated with an increment in the slope of the responsivity; thus, the sensitivity and q are inversely proportional. When one increases, the other decreases. In short, q is a trade-off parameter between the position of the working point and the sensitivity of the sensor

$$q \downarrow \implies z_{\text{TP}} \downarrow \text{ and } q \downarrow \implies S_{\max} \uparrow .$$

As previously stated, the working range is defined as $\Delta z_{5,65} = z_{65} - z_5$, which equals to $0.94\sqrt{q}$. This can easily be deduced by following the same procedure that led to (16) and (20). Thus, a larger working range of the sensor implies a larger value of q; which, in turn, decreases the sensitivity. In conclusion, the range of distances at which the responsivity is linear is inversely proportional to the sensitivity

$$q \uparrow \implies \Delta z_{5,65} \uparrow \text{ so, } \Delta z_{5,65} \uparrow \implies S(z) \downarrow .$$

This loss of sensitivity can be corrected, at least partially, in two ways.

a) Externally, increasing the gain of the photodetectors.
b) Increasing p as it is proportional to the sensitivity (15).

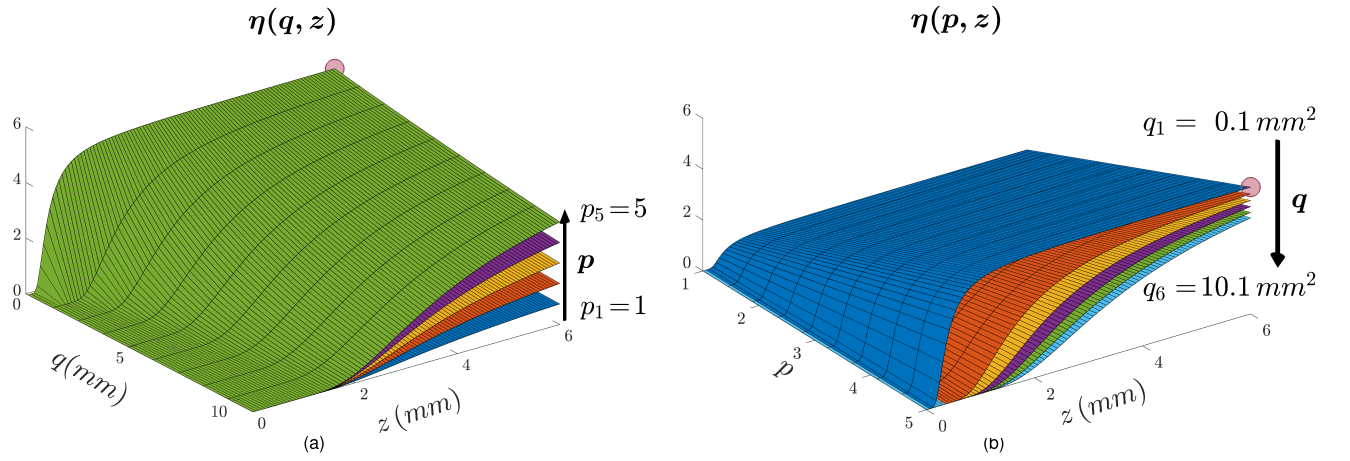

Fig. 6. Responsivity as a function of q and p. (a) Responsivity as a function of $\{q, z\}$ for different p, from $p = 1$ to 5 in steps of 1. The top green surface corresponds to $p = 5$ and the blue at the bottom to $p = 1$. (b) Responsivity as a function of p and z for different q, from $q = 0.1$ mm^2 to 10.1 mm^2 in steps of 2 mm^2. The top blue surface corresponds to $q = 0.1$ mm^2 and the cyan at the bottom to $q = 10.1$ mm^2. The red markers indicate the same point.

The maximum and minimum values of p are given by the size of the bundle, $R \geq \rho_2 + \Delta\rho_2$, and the size of the transmitting fiber, $r_T \leq \rho_1 - \Delta\rho_1$. For that purpose, to increase p, the outer receiving ring should either be wider, located further away, or both. From (13), widening the area of the outer ring or reducing the area of the inner ring leads to a larger p. This is possible while leaving q unchanged since they are independent. The only practical limitations of this procedure are the maximum gain of the photodetectors [k_i, (10)] and the maximum ratio of the areas of the receiving rings $p = A_2/A_1$, which, in summary, depend on both the size of the bundle R and the size of the emitting fiber r_T. Identical conclusions can be drawn from Fig. 6(b), which shows the sensitivity as a function of p and z for different values of q.

In summary, to achieve a wider working range and higher sensitivity, we need to increase $\{p, q\}$ in the sensor design. Moreover, a higher responsivity can be obtained by increasing p, see (13).

In a second analysis, we conducted a set of simulations to understand better the influence of each parameter by varying one while the rest remained fixed. Fig. 7 shows the results of the toy model for the responsivity $\eta(z)$ and sensitivity, $S(z)$. The reference parameters are

$$\begin{array}{ll} \rho_1 = 0.5 \text{ mm} & \rho_2 = 1.0 \text{ mm} \\ \Delta\rho_1 = 0.2 \text{ mm} & \Delta\rho_2 = 0.2 \text{ mm} \end{array} \quad \theta_0 = 5^\circ.$$

A. Variation of the Position of the Inner Ring ρ_1

This variation is equivalent to changing the position of the inner ring fibers. Looking at Fig. 7(a), we can hardly observe any change in the position of the sensitivity. This is because the range of values over which it can vary is small since the rest of the bundle limits the inner ring. However, the responsivity value drops sharply when we increase the value of ρ_1, bringing the two rings closer. This decrease of $\eta(z)$ is accompanied by a substantial drop in $S(z)$, see Fig. 7(b), and a variation of its maximum toward smaller values of z. The maximum value of the sensitivity is given at z_{TP} distance, $S_{\max} = S(z_{\text{TP}})$, substituting (16) in (15)

$$S(z_{\text{TP}}) = \frac{3\sqrt{3}\exp\left(-\frac{3}{2}\right)\rho_2\Delta\rho_2\tan\theta_0}{\rho_1\Delta\rho_1\sqrt{\rho_2^2 + \Delta\rho_2^2 - \rho_1^2 - \Delta\rho_1^2}}. \tag{21}$$

Also, the working range decreases slightly with an increase of ρ_1. So, as predicted by (16) and (21)

$$\rho_1 \uparrow \Longrightarrow z_{\text{TP}} \downarrow, S(z_{\text{TP}}) \downarrow, \Delta z_{5,65} \downarrow .$$

B. Variation of the Inner Ring Width $\Delta\rho_1$

The responsivity value is very sensitive to the width of the inner ring, as shown in Fig. 7(c). Increasing the width of the inner ring causes a significant decrease in the responsivity. When $\Delta\rho_1$ goes from [0.1, 3] mm, the responsivity divides by four. Fig. 7(d) depicts that the same is true for the sensitivity, which becomes three times smaller. In short, the responsivity decreases and flattens when the radius of the inner fibers increases. The position of $S(z_{\text{TP}})$, though, remains constant, meaning that q is less sensitive to changes in $\Delta\rho_1$. Likewise, the working range is independent of $\Delta\rho_1$. Summarizing

$$\Delta\rho_1 \uparrow \Longrightarrow \eta(z) \downarrow, S(z) \downarrow .$$

C. Variation of the Position of the Outer Radius ρ_2

If we modify the outer radius of the fiber ring, increasing the distance ρ_2, as shown in Fig. 7(e), we observe two effects on the responsivity. On the one hand, the curve shifts toward larger values of z; on the other hand, both its amplitude and working range increase. However, based on Fig. 7(f), there is a small decrease in sensitivity as ρ_2 increases. The position of its maximum value z_{TP} grows linearly with ρ_2. So

$$\rho_2 \uparrow \Longrightarrow q \uparrow, p \uparrow, \eta(z) \uparrow, z_{\text{TP}} \uparrow S(z) \downarrow .$$

This can be understood from (13) and (16). An increase of ρ_2 raises the value of q and p, and, therefore, z_{TP}. Hence, the maximum value of the responsivity is also augmented. (21) explains the slight decay of sensitivity as ρ_2 increases.

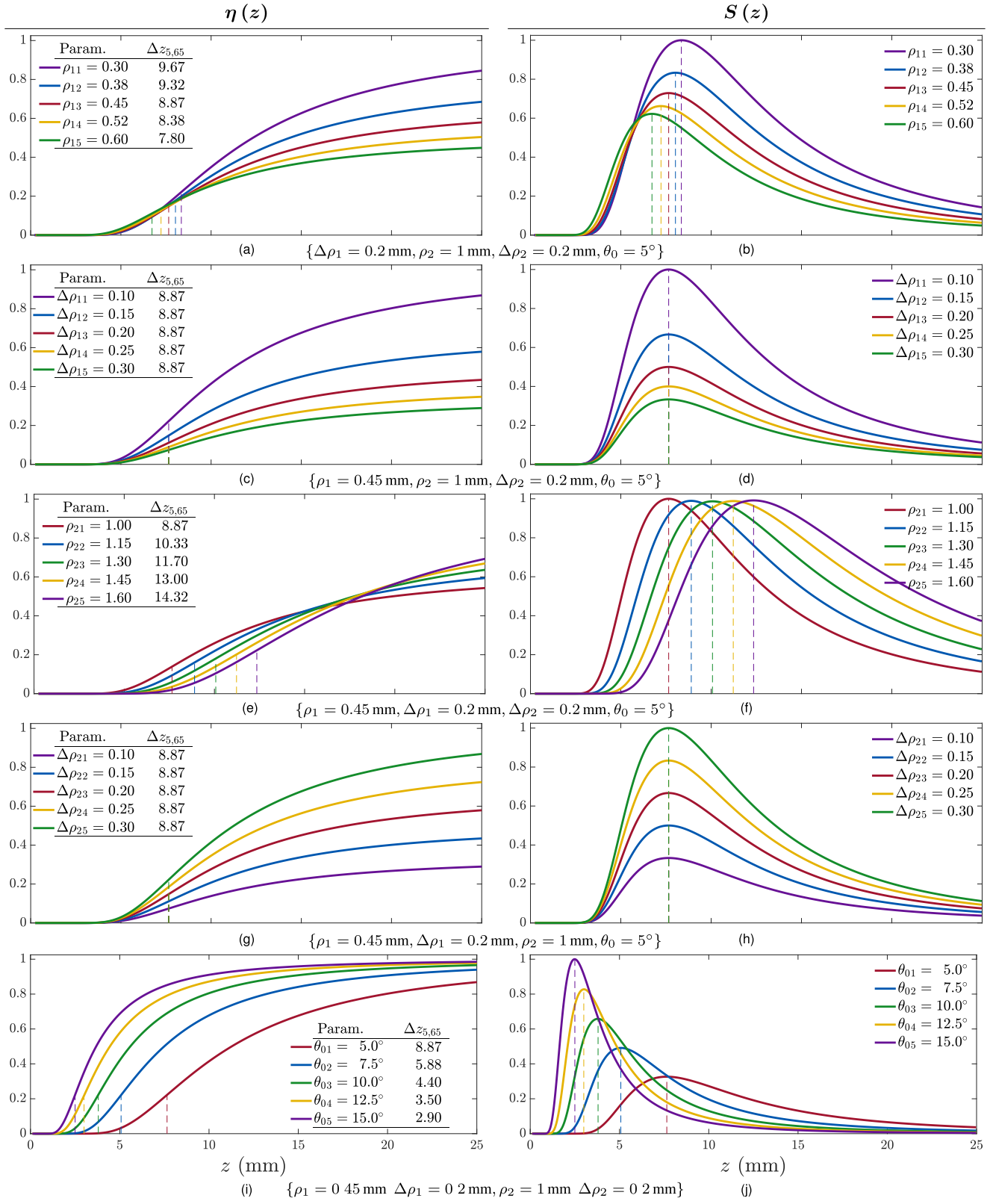

Fig. 7. All the values from the legends are in millimeters. Vertical lines show the z_{TP} points for every curve. (a) through (j) show the responsivity and sensitivity for five different geometrical parameter configurations: $\{\rho_1, \Delta\rho_1, \rho_2, \Delta\rho_2, \theta_0\}$. Data were normalized with respect to the maximum value.

D. Variation of the Outer Ring Width $\Delta\rho_2$

If we now look at the variation of the sensor response with the width of the outer ring, Fig. 7(g) and (h), we observe the opposite behavior. This is due to the minus sign in the q factor. By increasing the value of $\Delta\rho_2$ in the range $[0.1, 3]$ mm, we triple the value of both responsivity and sensitivity. As with $\Delta\rho_1$ (Section III-B), the position of the turning point z_{TP} hardly varies and can be considered constant for

TABLE I
LIST OF POSSIBLE WORKING POINTS OF THE SENSOR TOGETHER WITH THE VALUE OF THEIR RESPECTIVE RESPONSIVITIES

Working Point	Description	Numerical value	$\eta(z)$
z_{HM}	Distance at half maximum	$\sqrt{q/\ln 2} = 1.20\sqrt{q}$	$\eta(z_{\mathrm{HM}}) = 0.50p$
z_{TP}	Turning point	$\sqrt{\frac{2}{3}q} = 0.82\sqrt{q}$	$\eta(z_{\mathrm{TP}}) = 0.22p$
z_{MC}	Minimum of curvature	$\frac{1}{2}\sqrt{\frac{1}{3}\left(9+\sqrt{33}\right)q} = 1.11\sqrt{q}$	$\eta(z_{\mathrm{MC}}) = 0.44p$
z_5	Distance at 5% of maximum	$\sqrt{-q/\ln 0.05} = 0.58\sqrt{q}$	$\eta(z_5) = 0.05p$
z_{65}	Distance at 65% of maximum	$\sqrt{-q/\ln 0.65} = 1.52\sqrt{q}$	$\eta(z_{65}) = 0.65p$
z_{HR}	Distance at half range	$\frac{1}{2}(z_{5\%}+z_{65\%}) = 1.05\sqrt{q}$	$\eta(z_{\mathrm{HR}}) = 0.35p$
$z_{\eta_{\max}}$	Maximum responsivity	∞	$\eta_{\max} = p$

this $\Delta\rho_2$ range. The same happens with the working range. Then

$$\Delta\rho_2 \uparrow \implies \eta(z) \uparrow, S(z) \uparrow .$$

E. Variation of the Numerical Aperture NA = sin(θ_0)

The last parameter to vary is the numerical aperture of the source. In Fig. 7(i) and (j) we vary the NA between [0.1, 3], which corresponds to the acceptance angles $\theta_0 = [5, 15]^\circ$. If we increase the NA, the responsivity increases in slope and shifts toward smaller z values, see Fig. 7(j). Its value is almost quadrupled and the position of the maximum, i.e., the value of z_{TP}, is halved. It is noteworthy the huge dependence of the working range on NA; the working range is indeed divided by three. Consequently

$$\mathrm{NA} \uparrow \implies \eta(z) \uparrow, z_{\mathrm{TP}} \downarrow, S(z) \uparrow .$$

F. Dead Zone

Some authors define the *dead* [39] or *blind* [20] zone of an OFDS as the range of distances in which the responsivity is very small or zero. In Table I we show that the value z_5 for which the responsivity is 5% of its maximum value is $z_5 = 0.58\sqrt{q}$. This parameter indicates the point at which the responsivity starts to rise. It is evident that, in order to minimize the dead zone, q must be reduced.

As previously discussed, there are two approaches to address this issue: either by moving the receiver fiber rings, increasing ρ_1, and decreasing ρ_2; or by increasing the NA of the source. This is easy to understand in both cases; if we decrease the distance between the fiber rings to the center of the bundle, the reflected light reaches the two rings significantly due to their proximity to the transmitting fibers. Conversely, increasing the NA causes the light to scatter rapidly, reaching the receiving rings even at a short distance. This can easily be observed for the case of two equal fiber rings $\Delta\rho_1 = \Delta\rho_2$

$$q = \frac{\rho_2^2 - \rho_1^2}{2\tan^2\theta_0} = \frac{(\rho_2-\rho_1)(\rho_2+\rho_1)}{2\tan^2(\arcsin \mathrm{NA})}. \tag{22}$$

So

$$\mathrm{NA} \uparrow \vee (\rho_2-\rho_1) \downarrow \vee (\rho_2+\rho_1) \uparrow \implies \text{Dead zone} \downarrow.$$

The individual inspection of the parameters yields the following design tips.

1) To operate at small distances, we should either increase the NA of the source, bring the fiber rings closer, or decrease the fiber rings to bundle center distance.
2) Distances z_{TP}, z_{HM}, and z_{HR} give us information about the position of the responsivity curve (see Table I).
3) Sensitivity can be improved by decreasing the width of the inner ring (the radius of the inner fibers), or equivalently, increasing the width of the outer ring (the radius of the outer fibers).
4) The position working point is independent of the width of the rings, i.e., the diameter of the fibers.

IV. DESIGN PROCEDURE

Although the fiber bundle sensor has a simple principle and many outstanding advantages, most of the research has focused on the model and calculation of the response of a specific bundle, i.e., modeling the response of the bundle knowing a priori its geometric parameters and configuration [13], [14], [15], [16], [17], [18]. However, there is no research on the design of such bundles from given specifications. In other words, no procedure that relates the target distance and the working range to the fiber parameters and bundle configuration.

The ultimate goal is to determine $\{\rho_1, \rho_2, \Delta\rho_1, \Delta\rho_2\}$ from the design requirements, which are: the size of the bundle (outer radius R) and the working point, z_{WP}, the sensitivity, $S(z)$, and working range, Δz, of the OFDS

$$\underbrace{\begin{bmatrix} R \\ z_{\mathrm{WP}} \\ S(z_{\mathrm{WP}}) \\ \Delta z \end{bmatrix}}_{\substack{\text{Input} \\ \text{Design requirements}}} \rightarrow \begin{bmatrix} \text{Solve} \\ \text{design equations} \end{bmatrix} \rightarrow \underbrace{\begin{bmatrix} \rho_1 \\ 2\Delta\rho_1 \\ \rho_2 \\ 2\Delta\rho_2 \end{bmatrix}}_{\text{Toy model}} = \underbrace{\begin{bmatrix} R_1 \\ \phi_1 \\ R_2 \\ \phi_2 \end{bmatrix}}_{\substack{\text{Output} \\ \text{Experimental} \\ \text{Geometrical parameters}}} .$$

The procedure can be summarized in the following steps.

1) First, for practical reasons, it is usually necessary to set a maximum radius R of the bundle

$$R = \rho_2 + \Delta\rho_2 \quad \text{(first design equation)}. \tag{23}$$

2) Then, q is determined from the working point. If we consider the turning point of the responsivity as the working point, i.e., $z_{\mathrm{WP}} = z_{\mathrm{TP}} = \sqrt{2q/3}$, then the parameter q becomes fixed

$$q = \frac{3}{2} z_{\mathrm{TP}}^2 \quad \text{(second design equation)}. \tag{24}$$

Any alternative working point also sets the q parameter. In general, and as we have previously indicated, the relationship between the working point z_{WP} and the parameter q is of the form $z_{\mathrm{WP}} = h\sqrt{q}$, being h a numerical constant, see Table I.
These two conditions impose restrictions on the slope of the responsivity. Indeed

$$\Delta\rho_2 = R - \rho_2 \tag{25}$$

$$\Delta\rho_1 = \sqrt{\rho_2^2 + (R-\rho_2)^2 - \rho_1^2 - \frac{z_{\mathrm{WP}}^2 \tan^2\theta_0}{h^2}} \tag{26}$$

and then, by substituting (25) and (26) in (13)

$$p = \frac{\rho_2(R-\rho_2)}{\rho_1\sqrt{\rho_2^2 + (R-\rho_2)^2 - \rho_1^2 - \frac{z_{\mathrm{WP}}^2 \tan^2\theta_0}{h^2}}}. \tag{27}$$

3) We could set either the sensitivity, $S(z_{\mathrm{WP}})$, or the maximum value of the responsivity of the sensor. It is equivalent to fixing the value of p. This is the *third design equation*. With the choice of $\{p, q\}$ the responsivity of the sensor becomes fixed

$$\eta(z) = p\exp\left(-\frac{z_{\mathrm{WP}}^2}{h^2 z^2}\right) \quad \text{(third design equation)}. \tag{28}$$

All that remains is to determine from the three design equations the geometric values of the two rings, i.e., the sizes and placement of the fibers. Since we have four parameters $\{\rho_1, \rho_2, \Delta\rho_1, \Delta\rho_2\}$ and three conditions, the problem is underdetermined. We can leave the design based on a free parameter we can take at will, e.g., ρ_2. Expressing the three design equations as a function of ρ_2, we obtain

BUNDLE DESIGN COOKBOOK

$$\left[\begin{array}{ll} \Delta\rho_2 = R - \rho_2 & \text{(DE1)} \\ \Delta\rho_1 = \sqrt{\rho_2^2 + (R-\rho_2)^2 - \rho_1^2 - \frac{z_{\mathrm{WP}}^2 \tan^2\theta_0}{h^2}} & \text{(DE2)} \\ \rho_1 = \frac{\rho_2\Delta\rho_2}{p\Delta\rho_1} & \text{(DE3)} \end{array}\right].$$

A simple inspection of the latter brings two clues about the bundle design process. The smaller the radius of the inner ring ρ_1, the greater the intrinsic slope p of the responsivity, i.e., the greater the sensitivity. This would recommend placing the first ring as close as possible to the emitter fiber, establishing the new condition

$$r_T = \rho_1 - \Delta\rho_1 \tag{29}$$

$$\rho_1 = \frac{r_T}{2} \pm \sqrt{\frac{R^2}{2} - \frac{r_T^2}{4} - \frac{z_{\mathrm{WP}}^2 \tan^2\theta_0}{2h^2} - \rho_2^2 - R\rho_2}. \tag{30}$$

However, this choice is not always compatible with the selection of the working point or q. Notice that we can easily raise the chosen slope at the working point, $S(z_{\mathrm{WP}})$, by just tuning the asymmetric gain factor k, which is determined from the selected photodetectors gains as demonstrated in (11)

$$\left.\frac{d\eta(z)}{dz}\right|_{z_{\mathrm{WP}}} = S(z_{\mathrm{WP}}) = 2k\frac{p}{h^2 z_{\mathrm{WP}}}\exp\left(-\frac{1}{h^2}\right). \tag{31}$$

Two additional constraints must always be satisfied for the design to be physically feasible, namely

$$r_T \leq \rho_1 - \Delta\rho_1 \tag{32a}$$

$$\rho_2 \geq \rho_1 + \Delta\rho_1 + \Delta\rho_2. \tag{32b}$$

These inequalities only reflect that the rings in the toy model and the fibers in the experimental fiber bundle cannot overlap.

Another design option is to set a known linear response, $f(z) = z_0 + mz$, in a specified range, $[z_{\mathrm{i}}, z_{\mathrm{f}}]$ and find the responsivity that best approximates it within that range. Then, we look for the responsivity that minimizes the error in the working range of the sensor $[z_i, z_f]$. For the sake of ease of reading, the design equations for this case have been developed in the Appendix.

We shall illustrate the preceding procedure with two real-world examples, both of which are carefully discussed in Sections V-A and V-B.

V. Experimental Validation

The experimental setup has been described in detail previously in [34] and [35]. Regarding the light source, a laser module from Frankfurt Components (HSML-0660-20-FC, Frankfurt Laser Company, Friedrichsdorf, Germany) was employed. It had a nominal output power of 20 mW at 660 nm. An optical isolator (IOF-660, Thorlabs, Newton, NJ, US) was placed between the laser and the bundle to avoid reflections that could destabilize the light source. For the opto-electrical conversion, two Thorlabs PDA100A-EC photodetectors were used. Finally, the responsitivity is calculated as the quotient of the two obtained voltage signals, $\{V_1, V_2\}$ for Section V-A, and $\{V_1, V_3\}$ for Section V-B.

To validate our model, a tetrafurcated bundle was designed and fabricated, consisting of a single-mode transmitting fiber at its center and three concentric rings of multimode receiving fibers. The chosen emitting fiber was a single-mode fiber as reasoned in Section II. The fibers of the first two rings have the same diameter, 0.2 mm. However, the outer ring fibers are 0.34 mm in diameter. The total diameter of the bundle is 1.12 mm. A microscopic image of its cross section is shown in Fig. 8(b). The values of the position and radii of the fibers are presented in Table II.

This bundle allows one to validate twice the model. Firstly, we compare the responsivity of two rings (first and second)

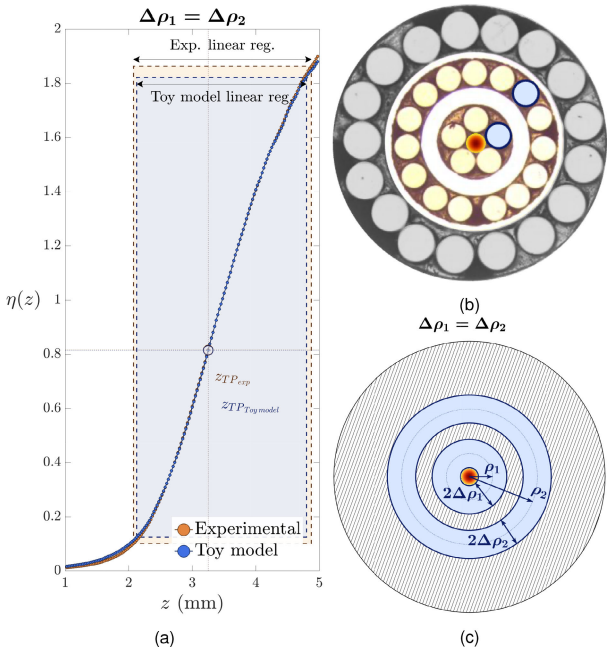

Fig. 8. (a) Responsivity according to Section V-A together with the experimental one from the bundle with identical receiving fibers. The toy model in blue, and the experimental in orange. For the toy model $k = k_2/k_1 = 1.8$. (b) Cross section of the manufactured bundle. (c) Cross section of the toy model.

with equal fibers (same ring width in the toy model). Secondly, we compare the responsivity of two rings of fibers with different diameters (the first and third rings, different ring widths in the toy model). Consequently, the validation consisted in comparing the responsivity of the toy model with the experimental one in both cases. To quantitatively compare the results in the working range, we calculated the mean square error (MSE) between the two responsivities. Furthermore, the points of interest defined in Table I were also compared, and the results are presented side-by-side in Table II.

TABLE II
SIDE-BY-SIDE COMPARISON OF THE OBTAINED RESULTS FOR THE TOY MODEL AND THE EXPERIMENTAL FIBER BUNDLE. MSE STANDS FOR MSE. THE OVERLAPPED WORKING RANGE IS DEFINED AS THE RANGE WHERE THE WORKING RANGE OF THE TOY MODEL AND THE EXPERIMENTAL BUNDLE COEXIST

VALIDATION SUMMARY					
EXAMPLE I				**EXAMPLE II**	
r_T (μm)	62			62	
R (μm)	700			1120	
Geometrical parameters (μm)					
ρ_{1_I}	297	R_{1_I}	324	$\rho_{1_{II}}$	297	$R_{1_{II}}$
$2\Delta\rho_{1_I}$	210	ϕ_{1_I}	200	$2\Delta\rho_{1_{II}}$	210	$\phi_{1_{II}}$
ρ_{2_I}	595	R_{2_I}	586	$\rho_{2_{II}}$	970	$R_{2_{II}}$
$2\Delta\rho_{2_I}$	210	ϕ_{2_I}	200	$2\Delta\rho_{2_{II}}$	387	$\phi_{2_{II}}$
Working range Δz (mm) *Pearson 0.997*					
2.12	2.07	z_i	2.52	2.17	
4.80	4.87	z_f	8.12	9.07	
2.67	2.80	Δz_r	5.60	6.90	
Working range Δz (mm) $[5, 65]$ %					
2.02	1.77	z_5	3.07	2.15	
3.87	3.07	z_{65}	6.45	6.05	
1.85	1.30	Δz	3.37	3.90	
Turning point z_{TP} (mm) *Max. sensibility*					
3.25	3.25		4.52	5.67	
Distance at half range z_{HR} (mm)					
3.12	2.65		5.45	4.45	
Distance at half maximum z_{HM} (mm)					
2.87	3.47		5.25	6.7	
MSE overlapped working range					
0.002%			1.300%		
MSE whole range					
1.112%			1.011%		

A. Example I

In this first example, we wanted to design a bundle with two equal diameter fiber rings, $\Delta\rho_1 = \Delta\rho_2$, with an outer radius $R = 0.7$ mm, $r_T = 0.062$ mm, $\theta_0 = 5°$. $z_{WP} = 5$ mm was chosen at the distance where the responsivity is half of its maximum value, z_{HM}. Let $p = 2$ and $z_{HM} = 5$ mm.

Fig. 8(b) and (c) illustrates the case. In this scenario (11) and (14) become as follows:

$$q = \frac{\rho_2^2 - \rho_1^2}{2\tan^2\theta_0}; \quad p = \frac{\rho_2}{\rho_1} \tag{33a}$$

$$\eta(z) = \frac{\rho_2}{\rho_1}\exp\left(-\frac{\rho_2^2 - \rho_1^2}{2z^2\tan^2\theta_0}\right). \tag{33b}$$

With the working point $q = z_{WP}^2/h^2$, and the limit p fixed by design, we calculate $\{\rho_1, \rho_2\}$ as a function of $\{p, q\}$. Indeed, clearing $\{\rho_1, \rho_2\}$ from (33a) and (33b), and taking (23)

$$\rho_1 = \sqrt{2}\tan\theta_0\sqrt{\frac{q}{p^2-1}} \tag{34a}$$

$$\rho_2 = p\sqrt{2}\tan\theta_0\sqrt{\frac{q}{p^2-1}} \tag{34b}$$

$$\Delta\rho_1 = \Delta\rho_2 = R - \rho_2. \tag{34c}$$

Solving the equations

$$\rho_1 = 297\ \mu\text{m}$$
$$\rho_2 = 595\ \mu\text{m}$$
$$\Delta\rho_1 = \Delta\rho_2 = R - \rho_2 = 105\ \mu\text{m}.$$

As mentioned before, we also must comply with the (32a) and (32b) geometrical constraints, assuring that the design can be truly fabricated. For (32a) geometrical constraint

$$\rho_{2,\min} = \rho_1 + 2\Delta\rho_1 = 507\ \mu\text{m}$$
$$\rho_2 = 595\ \mu\text{m} > 507\ \mu\text{m} \quad \checkmark$$

and for (32b) constraint

$$\rho_{1,\min} = r_T + \Delta\rho_1 = 167\ \mu\text{m}$$
$$\rho_1 = 297\ \mu\text{m} > 167\ \mu\text{m} \quad \checkmark.$$

So, the design is truly manufacturable.

B. Example II

In this second example, the receiving rings have different widths as depicted in Fig. 9(b) and (c) (the manufactured

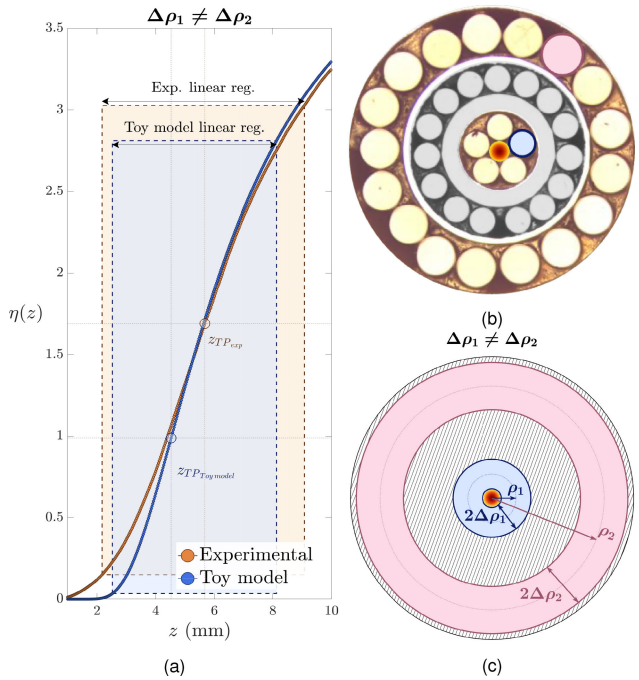

Fig. 9. (a) Responsivity according to Section V-B together with the experimental one from the bundle with receiving fibers of different diameters. The toy model in blue and the experimental in orange. For the toy model $k = k_2/k_1 = 1.15$. (b) Cross section of the manufactured bundle. (c) Cross section of the toy model.

bundle and the toy model). This time, we set the working point at $z_{\mathrm{WP}} = 4.4$ mm, and we will also assume that this point corresponds to the turning point $z_{\mathrm{WP}} = z_{\mathrm{TP}}$.

Taking $R = 1.12$ mm and $\rho_2 = 0.97$ mm, and also setting the maximum responsivity to $p = 4.5$, then

$$q = \frac{\rho_2^2 + \Delta\rho_2^2 - \rho_1^2 - \Delta\rho_1^2}{2\tan\theta_0^2} = \frac{3}{2} z_{\mathrm{TP}}^2 = 29 \text{ mm}^2$$

and

$$\rho_2^2 + \Delta\rho_2^2 - \rho_1^2 - \Delta\rho_1^2 = 0.85 \text{ mm}^2.$$

Moreover, $\Delta\rho_2 = R - \rho_2 = 0.15$ mm, and from the definition of p (13)

$$p = 4.5 = \frac{\rho_2(R - \rho_2)}{\rho_1 \Delta\rho_1} \Rightarrow \Delta\rho_1 = 0.032 \text{ mm}^2 \rho_1^{-1}.$$

Hence

$$0.97^2 \text{ mm}^2 + 0.15^2 \text{ mm}^2 - \rho_1^2 - 0.001 \text{ mm}^4 \rho_1^{-2} = 0.85 \text{ mm}^2.$$

Solving for ρ_1, we get $\rho_1 = 0.32$ mm and $\Delta\rho_1 = 0.1$ mm. The geometric parameters of the bundle are as presented in Table II. Like in Section V-A, before accepting the design as feasible, we must ensure it satisfies the geometrical constraints. For (32a) constraint

$$\rho_1 + \Delta\rho_1 + \Delta\rho_2 \leq \rho_2.$$

Indeed

$$\rho_2 = 0.97 \geq 0.57 \text{ mm} \quad \checkmark.$$

Next, the second geometrical constraint (32b) is checked taking into account that $r_T = 0.062$ mm

$$r_T \leq \rho_1 - \Delta\rho_1 = 0.22 \text{ mm} \quad \checkmark.$$

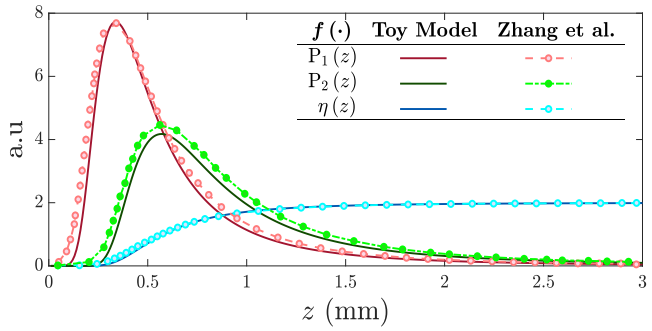

Fig. 10. Performance comparison between the bundle of Zhang et al. and the toy model taking $\{\rho_1 = 0.3, \Delta\rho_1 = 0.1, \rho_2 = 0.6, \Delta\rho_2 = 0.1\}$ mm and $\theta_0 = 37°$. The optical power collected by the inner ring (red) is $P_1(z)$, and the outer (green) is $P_2(z)$. The responsivities, $\eta(z)$, are in blue. Dashed lines represent the results of Zhang et al., and the continuous ones are the predicted by the toy model.

Finally, in Figs. 8(a) and 9(a), we present a comparison of the obtained two responsivities, namely, the one from the toy model in blue and the experimental from the manufactured bundle in orange. The toy model and experimental results are in very good agreement, with practically identical curves placed at the same working point.

Side-by-side results comparison of the two examples is presented in Table II. The geometrical parameters of the fabricated bundle are very close to those predicted by the model. The discrepancy between the toy model and the experimental curves of the responsivity can be quantified through the MSE, which is around 1% in the whole working range. This fact justifies the validity of the proposed toy model method.

Furthermore, we have calculated the working range of the toy model and the fabricated bundle in both examples. The working range was also defined as the region where Pearson's correlation coefficient exceeds 0.997. This value has already been used in the literature as a reference value [31], [32] and ensures the linearity of the working region. Table II also shows a strong degree of agreement, not only for the one calculated from Pearson's correlation coefficient but also from the proposed $[5, 65]\%$ range.

The most notable difference is observed in Example II (see Section V-B) for small distances, where the receiving fiber rings are more widely spaced. At small distances, the optical power gathered by the third ring is relatively low, leading to quantification errors in the measurements. These issues are not present in the ideal toy model.

Another advantage of using tetrafurcated OFDSs is that we can extend the linear range and increase the sensitivity by combining the responsivities of each pair of rings. Ultimately, we could further extend the OFDS range and steepness by using pentafurcated, hexafurcated OFDSs, etc. Nevertheless, that would inevitably lead to an increase in the overall size of the bundle. Hence, we should look for a trade-off between the desired linear range and the bundle size (23).

Our model has also been validated with results from other researchers. In particular, we used our model to successfully replicate the results of Zhang and Yang [41]. The bundle used by these authors consists of two identical fiber rings closely spaced; the fiber core radii are $\Delta\rho_1 = \Delta\rho_2 = 0.1$ mm. The position of the inner ring of fibers is at $\rho_1 = 0.3$ mm, while

the outer one is at $\rho_2 = 0.6$ mm from the bundle-center. The fiber acceptance angle is $\theta_0 = 37°$.

In Fig. 10, we show the optical power collected by the inner (red curve) and outer (green curve) rings along with the responsivity (blue curve). The continuous lines show our results, and the dashed are from Zhang et al. As it can be seen, the toy model accurately predicts the results from Zhang et al., despite the toy model is an approximation, and Zhang et al. used a quasi-Gaussian source.

All these results justify the validity and accuracy of the model and its suitability as a bundle design tool.

VI. Conclusion

This work presents a practical method of great importance for the design of trifurcated OFDS sensors. A procedure for designing OFDSs has been developed based on three equations that relate sensor specifications: working distance, range, sensitivity, and linear behavior, to the bundle geometry.

Two design examples have been presented along with the experimental results. These show that the developed method is simple, powerful, and accurate, with an MSE under 1% in the whole working range of the sensor. Additionally, the method has been validated using a bundle from the literature. The proposed method can be applied not only to trifurcated OFDS, but also to any bundle design with azimuthal symmetry. Consequently, the proposed method has no limitations and performs equally regardless of the input specifications.

It is important to point out that the toy model simplifies a bundle of adjacent fibers. Thus, the greater the fibers inter-spacing within the same ring, the greater the discrepancy between the experimental values and those predicted by the toy model. In summary, the toy model does not apply to bundle configurations where the receiving rings are spread rather than filled with fibers.

In future work, we intend to improve the designs of OFDS sensors by using tetrafurcated and pentafurcated OFDSs to increase the amplitude and linear range.

Appendix
Least Squares Minimization

As mentioned in Section IV, there is another design procedure. It consists of approximating the response of the sensor as close as possible to a given straight line. Setting a known linear response $f(z) = \eta_0 + mz$ within a range $[z_i, z_f]$ we want to find the responsivity $\eta(z)$ that most closely approximates it within that range, i.e., we seek the responsivity $\eta(z)$ that minimizes the error in the working range of the sensor $[z_i, z_f]$. The error function $E(p, q)$ is defined as

$$E(p,q) = \|\eta(z) - (\eta_0 + mz)\|^2 \tag{A35}$$

$$E(p,q) = \int_{z_i}^{z_f} [\eta(z) - (\eta_0 + mz)]^2 \, dz. \tag{A36}$$

Expanding

$$E(p,q) = \int_{z_i}^{z_f} \eta(z)^2 \, dz - 2\eta_0 \int_{z_i}^{z_f} \eta(z) \, dz - 2m \int_{z_i}^{z_f} z\eta(z) \, dz + \eta_0^2 (z_f - z_i) + m\eta_0 \left(z_f^2 - z_i^2\right) + \frac{1}{3} m^2 \left(z_f^3 - z_i^3\right) \tag{A37}$$

$$E(p,q) = p^2 \int_{z_i}^{z_f} \exp\left(-2\frac{q}{z^2}\right) dz - 2\eta_0 p \int_{z_i}^{z_f} \exp\left(-\frac{q}{z^2}\right) dz - 2mp \int_{z_i}^{z_f} z \exp\left(-\frac{q}{z^2}\right) dz + \eta_0^2 (z_f - z_i) + m\eta_0 \left(z_f^2 - z_i^2\right) + \frac{1}{3} m^2 \left(z_f^3 - z_i^3\right). \tag{A38}$$

To obtain the optimum fit, we need to minimize the error over p and q, i.e., we must find the values p and q for which

$$\frac{\partial E(p,q)}{\partial p} = \frac{\partial E(p,q)}{\partial q} = 0. \tag{A39}$$

Setting the partial derivatives equal to zero yields

$$\frac{\partial E(p,q)}{\partial p} = 2\left[p \int_{z_i}^{z_f} \exp\left(-2\frac{q}{z^2}\right) dz - \eta_0 \int_{z_i}^{z_f} \exp\left(-\frac{q}{z^2}\right) dz - m \int_{z_i}^{z_f} z \exp\left(-\frac{q}{z^2}\right) dz\right] = 0 \tag{A40}$$

$$\frac{\partial E(p,q)}{\partial q} = 2p\left[-p \int_{z_i}^{z_f} z^{-2} \exp\left(-2\frac{q}{z^2}\right) dz + \eta_0 \int_{z_i}^{z_f} z^{-2} \exp\left(-\frac{q}{z^2}\right) dz + m \int_{z_i}^{z_f} z^{-1} \exp\left(-\frac{q}{z^2}\right) dz\right] = 0. \tag{A41}$$

Now it is time to equal the p values from (A40) and (A41). But first, we have to rearrange (A40)

$$p \int_{z_i}^{z_f} \exp\left(-2\frac{q}{z^2}\right) dz = \eta_0 \int_{z_i}^{z_f} \exp\left(-\frac{q}{z^2}\right) dz + m \int_{z_i}^{z_f} z \exp\left(-\frac{q}{z^2}\right) dz \tag{A42}$$

so we can easily clear p from (A40)

$$p = \frac{\eta_0 \int_{z_i}^{z_f} \exp\left(-\frac{q}{z^2}\right) dz + m \int_{z_i}^{z_f} z \exp\left(-\frac{q}{z^2}\right) dz}{\int_{z_i}^{z_f} \exp\left(-2\frac{q}{z^2}\right) dz}. \tag{A43}$$

The exact process applies for clearing p from the partial derivative respect from q of the error function presented in (A41). First, we rearrange it

$$p \int_{z_i}^{z_f} z^{-2} \exp\left(-2\frac{q}{z^2}\right) dz = \eta_0 \int_{z_i}^{z_f} z^{-2} \exp\left(-\frac{q}{z^2}\right) dz + m \int_{z_i}^{z_f} z^{-1} \exp\left(-\frac{q}{z^2}\right) dz \tag{A44}$$

and then, we clear p from (A44) in order to equal it to the expression of p obtained in (A43)

$$p = \frac{\eta_0 \int_{z_i}^{z_f} z^{-2} \exp\left(-\frac{q}{z^2}\right) dz + m \int_{z_i}^{z_f} z^{-1} \exp\left(-\frac{q}{z^2}\right) dz}{\int_{z_i}^{z_f} z^{-2} \exp\left(-2\frac{q}{z^2}\right) dz}. \tag{A45}$$

Equaling the expressions of p from (A43) and (A45), we obtain

$$\frac{\eta_0 \int_{z_i}^{z_f} \exp\left(-\frac{q}{z^2}\right) dz + m \int_{z_i}^{z_f} z \exp\left(-\frac{q}{z^2}\right) dz}{\int_{z_i}^{z_f} \exp\left(-2\frac{q}{z^2}\right) dz}$$

$$= \frac{\eta_0 \int_{z_i}^{z_f} z^{-2} \exp\left(-\frac{q}{z^2}\right) dz + m \int_{z_i}^{z_f} z^{-1} \exp\left(-\frac{q}{z^2}\right) dz}{\int_{z_i}^{z_f} z^{-2} \exp\left(-2\frac{q}{z^2}\right) dz}. \tag{A46}$$

Coming to an end, all we have to do is solve (A46) for q for the selected slope m and the intersecting value η_0 of the line with the abscissa axis. Finally, we use equation (A43) or (A45) to obtain the value of p. Knowing $\{p, q\}$, we can proceed by following the steps listed in Section IV and get the fiber bundle design for the specific application.

REFERENCES

[1] J. L. Santos, "Optical sensors for Industry 4.0," *IEEE J. Sel. Topics Quantum Electron.*, vol. 27, no. 6, pp. 1–11, Nov. 2021.

[2] D. H. A. Munap, N. Bidin, S. Islam, M. Abdullah, F. M. Marsin, and M. Yasin, "Fiber optic displacement sensor for industrial applications," *IEEE Sensors J.*, vol. 15, no. 9, pp. 4882–4887, Sep. 2015.

[3] D. Sastikumar, G. Gobi, and B. Renganathan, "Determination of the thickness of a transparent plate using a reflective fiber optic displacement sensor," *Opt. Laser Technol.*, vol. 42, no. 6, pp. 911–917, Sep. 2010. [Online]. Available: https://linkinghub.elsevier.com/retrieve/pii/S0030399210000095

[4] J. Zubia, O. Aresti, J. Arrue, and M. Lopez-Amo, "Barrier sensor based on plastic optical fiber to determine the wind speed at a wind generator," *IEEE J. Sel. Topics Quantum Electron.*, vol. 6, no. 5, pp. 773–779, Oct. 2000.

[5] Z. Nan-nan and Z. Jun, "Surface roughness measurement based on fiber optic sensor," *Measurement*, vol. 86, pp. 239–245, May 2016. [Online]. Available: https://www.sciencedirect.com/science/article/pii/S0263224116001342

[6] I. García, R. Przysowa, J. Amorebieta, and J. Zubia, "Tip-clearance measurement in the first stage of the compressor of an aircraft engine," *Sensors*, vol. 16, no. 11, p. 1897, Nov. 2016. [Online]. Available: https://www.mdpi.com/1424-8220/16/11/1897

[7] Y. Ye, C. Zhang, C. He, X. Wang, J. Huang, and J. Deng, "A review on applications of capacitive displacement sensing for capacitive proximity sensor," *IEEE Access*, vol. 8, pp. 45325–45342, 2020. [Online]. Available: https://ieeexplore.ieee.org/document/9020070/

[8] B. George, Z. Tan, and S. Nihtianov, "Advances in capacitive, eddy current, and magnetic displacement sensors and corresponding interfaces," *IEEE Trans. Ind. Electron.*, vol. 64, no. 12, pp. 9595–9607, Dec. 2017.

[9] S. A. Pullano, C. D. Critello, M. G. Bianco, M. Menniti, and A. S. Fiorillo, "PVDF ultrasonic sensors for in-air applications: A review," *IEEE Trans. Ultrason., Ferroelectr., Freq. Control*, vol. 68, no. 7, pp. 2324–2335, Jul. 2021.

[10] G. Berkovic and E. Shafir, "Optical methods for distance and displacement measurements," *Adv. Opt. Photon.*, vol. 4, no. 4, p. 441, Dec. 2012. [Online]. Available: https://opg.optica.org/aop/abstract.cfm?uri=aop-4-4-441

[11] K.-E. Peiponen, R. Myllylä, and A. V. Priezzhev, *Optical Measurement Techniques: Innovations for Industry and the Life Sciences*. Berlin, Germany: Springer, Feb. 2009. [Online]. Available: https://google-Books-ID:UFIzj6n9JHsC.

[12] J. M. López-Higuera, *Handbook of Optical Fibre Sensing Technology*. New York, NY, USA: Wiley, 2002.

[13] I. García et al., "Different configurations of a reflective intensity-modulated optical sensor to avoid modal noise in tip-clearance measurements," *J. Lightw. Technol.*, vol. 33, no. 12, pp. 2663–2669, Jun. 15, 2015. [Online]. Available: http://ieeexplore.ieee.org/document/7024913/

[14] L. Yuan, "Automatic-compensated two-dimensional fiber-optic sensor," *Opt. Fiber Technol.*, vol. 4, no. 4, pp. 490–498, Oct. 1998. [Online]. Available: https://linkinghub.elsevier.com/retrieve/pii/S1068520098902668

[15] M. Yasin, S. W. Harun, H. A. Abdul-Rashid, and H. Ahmad, "The performance of a fiber optic displacement sensor for different types of probes and targets," *Laser Phys. Lett.*, vol. 5, no. 1, pp. 55–58, Jan. 2008. [Online]. Available: https://iopscience.iop.org/article/10.1002/lapl.200710080

[16] G. Zubia Garea, J. Amorebieta, J. Zubia, and G. Durana, "An algorithm to optimize the optical sensor design for tip clearance and tip timing measurements," *Proc. SPIE*, vol. 12139, pp. 194–200, May 2022. [Online]. Available: https://www.spiedigitallibrary.org/conference-proceedings-of-spie/12139/2624373/An-algorithm-to-optimize-the-optical-sensor-design-for-tip/10.1117/12.2624373.full

[17] D. Ye, F. Duan, J. Jiang, G. Niu, Z. Liu, and F. Li, "Identification of vibration events in rotating blades using a fiber optical tip timing sensor," *Sensors*, vol. 19, no. 7, p. 1482, Mar. 2019. [Online]. Available: https://www.mdpi.com/1424-8220/19/7/1482

[18] G. He and F. W. Cuomo, "Displacement response, detection limit, and dynamic range of fiber-optic lever sensors," *J. Lightw. Technol.*, vol. 9, no. 11, pp. 1618–1625, Nov. 1991. [Online]. Available: http://ieeexplore.ieee.org/document/97654/

[19] L. Yuan, "A novel fiber-optic slide-sensing scheme," *Opt. Fiber Technol.*, vol. 7, no. 4, pp. 340–349, Oct. 2001. [Online]. Available: https://linkinghub.elsevier.com/retrieve/pii/S1068520001903621

[20] P. B. Buchade and A. D. Shaligram, "Influence of fiber geometry on the performance of two-fiber displacement sensor," *Sens. Actuators A, Phys.*, vol. 136, no. 1, pp. 199–204, May 2007. [Online]. Available: https://www.sciencedirect.com/science/article/pii/S0924424706007266

[21] P. B. Buchade and A. D. Shaligram, "Simulation and experimental studies of inclined two fiber displacement sensor," *Sens. Actuators A, Phys.*, vol. 128, no. 2, pp. 312–316, Apr. 2006. [Online]. Available: https://linkinghub.elsevier.com/retrieve/pii/S0924424706001087

[22] J. B. Faria, "A theoretical analysis of the bifurcated fiber bundle displacement sensor," *IEEE Trans. Instrum. Meas.*, vol. 47, no. 3, pp. 742–747, Jun. 1998. [Online]. Available: http://ieeexplore.ieee.org/document/744340/

[23] P. Puangmali, K. Althoefer, and L. D. Seneviratne, "Mathematical modeling of intensity-modulated bent-tip optical fiber displacement sensors," *IEEE Trans. Instrum. Meas.*, vol. 59, no. 2, pp. 283–291, Feb. 2010. [Online]. Available: http://ieeexplore.ieee.org/document/5229170/

[24] R. Lloyd. (Jul. 2023). *Displacement Measurement by Fiber Optics*. [Online]. Available: https://vitrek.com/applications/fiber-optic-displacement-measurement/

[25] H. Cao, Y. Chen, Z. Zhou, and G. Zhang, "Theoretical and experimental study on the optical fiber bundle displacement sensors," *Sens. Actuators A, Phys.*, vol. 136, no. 2, pp. 580–587, May 2007. [Online]. Available: https://linkinghub.elsevier.com/retrieve/pii/S0924424706007631

[26] T. Lan, C. Zhang, S. Fu, B. Zhu, M. Tang, and W. Tong, "Spatial division multiplexing-based reflective intensity-modulated fiber optics displacement sensor," *IEEE Photon. J.*, vol. 10, no. 4, pp. 1–7, Aug. 2018. [Online]. Available: https://ieeexplore.ieee.org/document/8392431/

[27] V. Kleiza and J. Verkelis, "Regularities of signal and sensitivity variation of a reflection fiber optopair sensor dependent on the angle between axes of fiber tips," *Nonlinear Anal., Model. Control*, vol. 14, no. 1, pp. 41–49, Jan. 2009. [Online]. Available: http://www.journals.vu.lt/nonlinear-analysis/article/view/14529

[28] D. Sagrario and P. Mead, "Axial and angular displacement fiber-optic sensor," *Appl. Opt.*, vol. 37, no. 28, p. 6748, Oct. 1998. [Online]. Available: https://opg.optica.org/abstract.cfm?URI=ao-37-28-6748

[29] A. Khiat, F. Lamarque, C. Prelle, N. Bencheikh, and E. Dupont, "High-resolution fibre-optic sensor for angular displacement measurements," *Meas. Sci. Technol.*, vol. 21, no. 2, Feb. 2010, Art. no. 025306. [Online]. Available: https://iopscience.iop.org/article/10.1088/0957-0233/21/2/025306

[30] B. Jia, L. He, G. Yan, and Y. Feng, "A differential reflective intensity optical fiber angular displacement sensor," *Sensors*, vol. 16, no. 9, p. 1508, Sep. 2016. [Online]. Available: http://www.mdpi.com/1424-8220/16/9/1508

[31] G. Durana et al., "Design, fabrication and testing of a high-sensitive fibre sensor for tip clearance measurements," *Sensors*, vol. 18, no. 8, p. 2610, Aug. 2018. [Online]. Available: http://www.mdpi.com/1424-8220/18/8/2610

[32] I. García, J. Beloki, J. Zubia, G. Aldabaldetreku, M. Illarramendi, and F. Jiménez, "An optical fiber bundle sensor for tip clearance and tip timing measurements in a turbine rig," *Sensors*, vol. 13, no. 6, pp. 7385–7398, Jun. 2013. [Online]. Available: https://www.mdpi.com/1424-8220/13/6/7385

[33] R. S. Laddha, P. B. Buchade, and A. D. Shaligram, "Optimization of fiber radius and sensor probe-reflector distance of trifurcated fiber optic angular displacement sensor," in *Proc. AIP Conf.*, 2018, Art. no. 020022. [Online]. Available: https://pubs.aip.org/aip/acp/article/659378

[34] R. Fernández-Bello et al., "Performance comparison of three fibre-based reflective optical sensors for aero engine monitorization," *Sensors*, vol. 19, no. 10, p. 2244, May 2019. [Online]. Available: https://www.mdpi.com/1424-8220/19/10/2244

[35] R. Fernández, J. Amorebieta, I. García, G. Aldabaldetreku, J. Zubia, and G. Durana, "Review of a custom-designed optical sensing system for aero-engine applications," *Int. J. Turbomachinery, Propuls. Power*, vol. 6, no. 1, p. 3, Feb. 2021. [Online]. Available: https://www.mdpi.com/2504-186X/6/1/3

[36] J. M. S. Sakamoto, G. M. Pacheco, C. Kitano, and B. R. Tittmann, "Geometrical parameter analysis of a high-sensitivity fiber optic angular displacement sensor," *Appl. Opt.*, vol. 53, no. 36, p. 8436, Dec. 2014. [Online]. Available: https://opg.optica.org/abstract.cfm?URI=ao-53-36-8436

[37] A. Shimamoto and K. Tanaka, "Geometrical analysis of an optical fiber bundle displacement sensor," *Appl. Opt.*, vol. 35, no. 34, p. 6767, Dec. 1996. [Online]. Available: https://opg.optica.org/abstract.cfm?URI=ao-35-34-6767

[38] S. S. Patil, "FOS explore—A new design optimization tool for fiber optic displacement sensor," in *Proc. AIP Conf.*, 2021, Art. no. 090003. [Online]. Available: https://pubs.aip.org/aip/acp/article/1000732

[39] H. Huang and U. Tata, "Simulation, implementation, and analysis of an optical fiber bundle distance sensor with single mode illumination," *Appl. Opt.*, vol. 47, no. 9, pp. 1302–1309, Mar. 2008. [Online]. Available: https://opg.optica.org/abstract.cfm?URI=ao-47-9-1302

[40] B. E. A. Saleh and M. C. Teich, *Fundamentals of Photonics*. Hoboken, NJ, USA: Wiley, Feb. 2019. [Online]. Available: https://google-Books-ID: rcqKDwAAQBAJ.

[41] X. Zhang and L. Yang, "Research on displacement sensor of two-circle reflective coaxial fiber bundle," in *Proc. IEEE/ASME Int. Conf. Adv. Intell. Mechatronics*, Jul. 2008, pp. 211–216. [Online]. Available: https://ieeexplore.ieee.org/document/4601661/

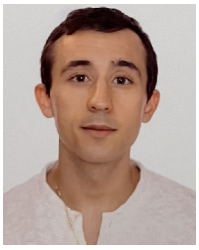

Gorka Zubia (Graduate Student Member, IEEE) was born in Barakaldo, Spain, in 1996. He received the B.Sc. (Hons.) and M.Sc. degrees in telecommunications engineering from the University of the Basque Country (UPV/EHU), Bilbao, Spain, in 2021, where he is now pursuing the Ph.D. degree in photonics.

Since 2023, he has been a Non-Doctoral Assistant Professor with the Department of Applied Mathematics at the UPV/EHU. His research interests focuses in mathematical modeling, designing and manufacturing fiber optic sensors for measuring physical parameters and structural health monitoring.

Dr. Zubia was awarded the Ikasiker Research Collaboration Fellowship by the Basque Government (Spain). He was honored with the Predoctoral Fellowship of the Basque Government to conduct his Ph.D. research within the Applied Photonics Group (APG) at the UPV/EHU.

Joseba Zubia (Member, IEEE) was born in Barakaldo, Spain, in 1965. He received the M.Sc. and Ph.D. degrees in physics from the University of the Basque Country (UPV/EHU), Bilbao, Spain, in 1988 and 1993, respectively.

Since 2001, he has been a Professor within the Department of Communications Engineering of the University of the Basque Country. He is the Founder and the Director of the Applied Photonics Group, recognized as outstanding by the Basque Science System. In this field, he has collaborated with leading European, Japanese, and U.S. researchers, and he has published over 150 articles in SCI-IF journals and contributed over 250 communications in scientific conferences. His research interests include developing fiber-optic sensors, fabricating polymer optical fibers, and quantum optics.

Dr. Zubia received a Special Award for the best thesis and the Euskoiker Research Award.

Josu Amorebieta received the M.Sc. and Ph.D. degrees in telecommunications engineering from the University of the Basque Country (UPV/EHU), Bilbao, Spain, in 2016 and 2021, respectively.

Afterward, he continued his research career in the Applied Photonics Group from the University of the Basque Country (UPV/EHU). Nowadays, he is a Lecturer with the Department of Applied Mathematics in the Bilbao School of Engineering of University of the Basque Country (UPV/EHU). His research fields involve the mathematical modeling, design, fabrication and validation of photonic sensors for several industrial applications such as the aeronautical industry.

Gotzon Aldabaldetreku received the M.Sc. and Ph.D. degrees in telecommunications engineering from the University of the Basque Country (UPV/EHU), Bilbao, Spain, in 2000 and 2006, respectively.

He is currently an Associate Professor with the Department of Communications Engineering, Bilbao School of Engineering, University of the Basque Country (UPV/EHU). His research interests include the development of fiber-optic sensors and fabrication of polymer optical fibers.

Dr. Aldabaldetreku was awarded for the best academic record in the M.Sc. degree and received a European acknowledgment for the Ph.D. degree and a Special Award for the Best Thesis.

Gaizka Durana received the B.Sc. degree in solid-state physics and the Ph.D. degree in engineering from the University of the Basque Country (UPV/EHU), Bilbao, Spain, in 1999 and 2008, respectively.

He is currently an Associate Professor with the Department of Communications Engineering, University of the Basque Country (UPV/EHU). His Ph.D. work received a European acknowledgment and focused on the experimental and numerical analysis of fundamental aspects of light propagation in multimode optical fibers. His current research interests include the manufacture of specialty polymer optical fibers, and the design, development and application of fiber-based optical sensors.